Contents lists available at ScienceDirect

Applied Surface Science

journal homepage: www.elsevier.com/locate/apsusc

Full length article

Laser nanostructured metasurfaces in Nb superconducting thin films

Antonio Badía-Majós [a,*], Elena Martínez [a], Luis A. Angurel [a], Germán F. de la Fuente [a], Emile Fourneau [b], Stefan Marinković [b], Alejandro V. Silhanek [b]

[a] Instituto de Nanociencia y Materiales de Aragón (INMA), CSIC-Universidad de Zaragoza, Zaragoza, Spain
[b] Experimental Physics of Nanostructured Materials, Q-MAT, CESAM, Univ. de Liège, Liège, Belgium

ARTICLE INFO

Dataset link: https://doi.org/10.5281/zenodo.10245401

Keywords:
Laser Induced Periodic Surface Structures
Magnetic flux penetration
Critical current density
Dendritic avalanches

ABSTRACT

Superconducting Nb thin films have been nanostructured by means of a femtosecond UV laser. Laser induced periodic surface structures (LIPSS) with lateral modulation of ≈ 250 nm and depth smaller than amplitude (≲ 20 nm from crest to trough) are obtained for optimized laser scanning conditions over the film surface, i.e. power, frequency, scanning speed and polarization. This provides a fast and scalable procedure of surface control at the nanoscale. In thin films, control over the kinetics of the LIPSS formation process has been crucial. Untreated and laser-patterned samples have been characterized by electron and atomic force microscopy as well as by local and global magnetometry. The superconducting properties reveal anisotropic behavior in accordance with the observed topography. The imprinted LIPSS define channels for anisotropic current flow and flux penetration. At low temperatures, magnetic flux avalanches are promoted by the increased critical current density, though flux tends to be channeled along the LIPSS. In general, directional flux penetration is observed, being a useful feature in fluxonic devices. Scalability allows us to pattern areas of the order of cm^2/min.

1. Introduction

Superconductivity in Nb metal has attracted much attention over decades and interest still remains. Remarkably, this transition metal classifies as type-I/type-II superconductor depending on the absence/presence of disorder in the samples (most frequently occurring in the form of impurities, defects, geometrical limitations or stress). On the other hand, it displays the highest critical parameters among type-II superconducting pure elements ($T_c \approx 9$ K, $\mu_0 H_c(T \to 0) \approx 0.2$ T) [1,2]. In the field of applications, it has become a reference material in superconducting radio-frequency accelerator cavities, cryogenic microelectronics, superconducting transmission lines, and quantum computing technologies (see Refs. [3,4] and references therein for a recent update).

Here, we will concentrate on Nb thin films that fall into the type-II category. In particular, we put our focus on the fundamental issue of tailoring the dynamics of magnetic flux. As it is well known, in spite of the ability to support high magnetic fields and currents in static conditions, superconductors suffer detrimental dissipation effects under dynamic conditions. More specifically, unpinned quantum flux units (so-called fluxons or vortices) drifting across the sample give way to irreversible energy losses. On occasion, such losses may reach dramatic levels when abrupt bursts of magnetic flux take the form of avalanches temporarily driving part of the sample into the normal state. Thus, effective strategies to mitigate the above phenomena are continuously investigated. Although, very different in nature, artificial defects created by chemical doping or irradiation, voids (also called antidots), magnetic inclusions, etc, [5] share the common feature that typically, their effectiveness relies on them matching the characteristic scale lengths of the superconducting condensate (submicron range). It is under such conditions that they may act as barriers able to channel the movement of fluxons. Remarkably, the posibility of guiding fluxons in microelectronic superconducting devices is an established field of research (*fluxonics*), already envisaged in the early 90's [6] and, at present, enabled by the development of nanofabrication techniques. Thus, moving fluxons in a superconducting film under perpendicular magnetic field provides a dual technology alternative to the semiconductor electronics, while offering advantages such as the possibility of building high-speed and low power devices. In particular, solutions based on nanopatterned films, and with Nb playing a prominent role are being explored. As a basic concept, the introduction of surface patterns (grooves, magnetic stripes, shaped holes) in the submicron scale has enabled the fabrication of prototypes of fluxonic devices such as rectifiers, filters or triodes [7–9]. So far, the vast majority of the approaches to achieve accurate control of the reported surface

* Corresponding author.
E-mail address: anabadia@unizar.es (A. Badía-Majós).

https://doi.org/10.1016/j.apsusc.2023.159164
Received 26 September 2023; Received in revised form 1 December 2023; Accepted 15 December 2023

patterns have been based on the focused ion beam or e-beam litography techniques.

In this article, we put forward an alternative method for functionalizing superconducting Nb thin films, based on the irradiation of the sample with ultra-short laser pulses. This technique, already foreseen in the middle sixties and recently revived by virtue of the progress of laser technologies, has been recognized as an amazingly flexible, one-step, chemical-reaction-free, and easily scalable procedure of surface patterning [10–14]. In brief, upon selection of the relevant parameters (pulse duration, amount of energy deposited, laser wavelength and polarization, beam scanning speed and mode), it is possible to produce a corrugation of the surface in the form of parallel structures with lateral periodicity in the submicron range (Laser Induced Periodic Surface Structures, abbreviated as LIPSS, also called ripples). We recall that this approach has been applied with success to the case of metals, semiconductors, and polymers. Its fundamental mechanism is the selective energy deposition on the surface of the material via radiation interference phenomena. In the case of wide band-gap glasses and ceramic materials, advances have been hindered by intrinsic limitations, i.e.: the less efficient energy absorption in single-photon processes [14]. Recent progress on the patterning of these materials by laser scanning was reported in Ref. [15]. Generally speaking, a pre-requisite to provide successful results is a negative real part of the dielectric permittivity for the material [16] which in the end, may also determine the selection of the laser wavelength. On top of this, one must setup the incident radiation so as to activate the process in a surface layer, a fact that occurs in a range typically close to the ablation threshold. Customarily, the protocol is established as a feedback process between laser treatment and scanning electron microscopy (SEM) observation and analysis, changing conditions and so on. As shown by several authors [13,17], double pulse strategies are most effective to achieve reproducible modifications of the sample surface. In brief, the first incidence sets up the material, and the second pulse defines the periodic structure, i.e.: two-step irradiation on a given spot, or overlapping scans, induce more than a simple accumulation effect.

Outstandingly, tayloring of surfaces through the imprint of submicrometric structures has already provided applications in a large diversity of fields, sharing the property that certain physical phenomenon exhibits a characteristic length scale matching the artificially induced modulation. Commensurability between the physical length scale and a metasurface with periodic landscape has led to intense activity in the control of light diffraction related effects such as iridiscence of surfaces, wetting control (hydrophobic/-philic surfaces), cell growth or tribological applications [13]. As for the case of superconducting materials, the fundamental role of the characteristic lengths (penetration depth λ_L and coherence length ξ) has motivated incipient research [18–20], specifically for metalls and alloys due to the metallic character (that promotes the LIPSS formation phenomenon [17], allegedly through the formation of surface plasmon-polaritons) and for having λ_L, ξ in the range of tens or hundreds of nanometers.

For the case of superconducting Nb films, and relying on a variety of experimental observations, we have investigated the formation of LIPSS and the subsequent modulation of the physical properties. Our work builds upon the previous experience with bulk and Nb sheets of thickness $d \gtrsim 25\,\mu m$ [19,20]. In those references, it was shown that Nb is a valid candidate for the fabrication of LIPSS, and subsequent modification of superconducting properties, by means of ultra-short laser pulses. This paved the path for the current investigation but left a challenging open question. Indeed, according to the Atomic Force Microscopy (AFM) profiles obtained in Ref. [19], the emerging ripple structures were characterized by a lateral periodicity $\Lambda_{LIPSS} \approx 250\,nm$ and depth of similar value. Now, being focused on thin films (thickness down to 100 nm in this study), the question remains whether one may obtain connected structures with shallow grooves much wider than deeper or, on the contrary, a set of disconnected superconducting islands upon the substrate. In fact, as argued in Ref. [14], surface patterning of thin films by means of the *conventional* LIPSS technique is hindered by intrinsic limitations. In particular, the simultaneous independent control of lateral period and depth is indeed a difficult task which depends both, on materials fundamental properties and on the interplay between the different laser irradiation parameters applied [21]. Specifically, this article provides a contribution to the understanding of the influence of the laser irradiation protocol on the kinetics of the formation of LIPSS and their influence on the material's magnetic response as compared to the pristine films.

2. Experimental details

2.1. Fabrication of the films

Nb thin films (of thicknesses 100 nm and 200 nm) were deposited on top of Si/SiO_2 substrates ($275 \pm 25\,\mu m$ Si, 300 ± 25 nm SiO_2) using radio-frequency magnetron sputtering. The evaporation chamber was previously pumped down to 10^{-8} mbar and the Nb deposition was performed at a rate of 0.1 nm/s in Ar pressure of 5.3 mbar. Without breaking the vacuum, the samples were capped with a 7 nm-thick Al layer by electron beam evaporation. The thickness of the Al capping layer has been chosen to be slightly thicker than the native oxide layer of Al, [22] so it acts as a protective layer for Nb.

2.2. Laser patterning

Laser patterning of the thin films was performed by irradiating in air atmosphere with a fs UV $Yb:KGd(WO_4)_2$ [Yb:KGW] laser (Light Conversion, Vilnius, Lithuania), (Carbide CB3-40W). The main characteristic parameters of the radiation used are: (i) pulse duration $\tau_p = 238\,fs$, (ii) central wavelength $\lambda = 343\,nm$, (iii) pulse repetition $f_{rep} = 20\,kHz$, (iv) oscillator frequency $f_{osc} = 200\,kHz$, and (v) $1/e^2$ beam diameters $2a \times 2b = 36 \times 60\ \mu m^2$. The $1/e^2$ beam diameters were determined in the sample processing plane by using the so-called D2-method proposed by Liu [23].

For subsequent investigations, and prior to the laser treatment of the film surfaces, samples with size $3 \times 3\ mm^2$ were cut from the original films by laser machining and eventual cleavage. A pulsed green laser ($\tau_p = 249\,fs$, $\lambda = 515\,nm$) was used with pulse repetition frequency $f_{rep} = 10\,kHz$, in order to minimize damage by heat accumulation in the film. As concluded from electron microscopy observations, damage restricts to a width of a few micrometers along the perimeter, thus allowing to consider the dimensions of the superconducting platelet practically unaltered.

2.3. Electron microscopy

Microstructural characterization of the surface was performed using a MERLIN field-emission scanning electron microscope (FE-SEM) (Carls-Zeiss, Jena, Germany) equiped with an energy dispersive X-ray spectroscopy (EDS) system (Oxford Instruments, Abingdon, UK) operated at 5 kV, using Secondary Electron (SE), in-lens secondary electron and Energy Selective Backscattered (ESB) detectors.

The topography of cross sectional areas of the samples was analyzed by scanning Transmission Electron Microscopy (TEM) using a Tecnai F30 microscope (FEI company, Hillsboro, OR, USA). Sample preparation was performed with a Focused Ion Beam (FIB) in a Dual Beam Helios 650 (FEI company, Hillsboro, OR, USA). Prior to the preparation of the lamella, a protective carbon coating was deposited on the region of interest.

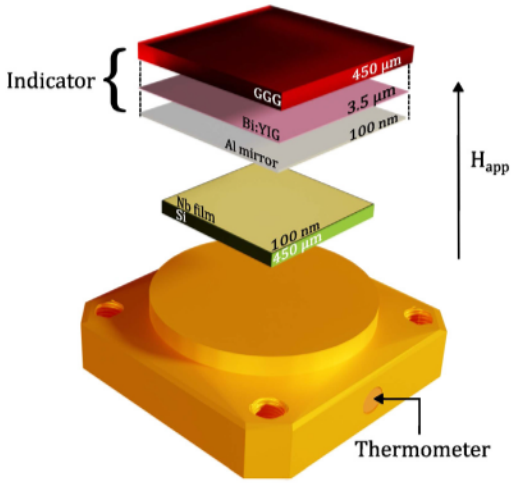

Fig. 1. Sketch of the setup employed in the MOI experiments. The square superconducting film (100 nm thick in this image) lies on the $XY-$ plane and a uniform magnetic field is applied along the $Z-$ axis. The sample placement geometry and the optically active indicator are depicted. The same perpendicular configuration (field along $Z-$ axis) was used in the SQUID magnetization measurements.

2.4. Atomic Force Microscopy (AFM)

The AFM profiles of the LIPSS were investigated using a Drive Nanosurf AFM and super-sharp silicon tips (SSS-NCHR from Nanoworld) with a typical curvature radius of 2 nm and a spring constant of 42 N/m. Measurements were conducted in tapping mode at a driven frequency of 275 kHz. Post-processing was carried out using the open-source software Gwyddion.

2.5. Magneto-optical Imaging (MOI)

The setup is based on a commercial polarization microscope. The light beam produced by a LED lamp is passed through a green filter (550 nm), then crosses a linear polarizer, and is then directed to the Faraday active indicator through the objective by a beam splitter. The indicator we use throughout this work is a 3.5 μm thick Bi-doped yttrium iron garnet (Bi:YIG) epitaxially grown on a 450 μm thick $Gd_3Ga_5O_{12}$ (GGG) transparent substrate. A 100 nm thick Al mirror was deposited on the optically active layer side in order to ensure sufficient reflection of the incident light beam. The linearly polarized light crosses the GGG substrate of the indicator and the Bi:YIG layer, where its polarization direction is rotated proportionally to the out-of-plane component of the local magnetic field. It is then reflected by the mirror and crosses the indicator and the objective once again. It subsequently passes through an analyzer, whose polarization direction is oriented close to 90° with respect to the polarizer. The rotation of the polarization is proportional to the component of the magnetic moment along the direction of light propagation. Light finally enters a high resolution CCD-camera mounted on top of the microscope unit. The sample is installed on an oxygen-free copper cold finger enclosed by a radiation shield, in a closed-cycle He cryostat. The whole microscope and the cryostat are mounted on an actively damped non-magnetic optical table. More details of the specific setup can be found in Ref. [24]. The specific position of the sample and the above mentioned layers, as well as their arrangement relative to the applied magnetic field are shown in Fig. 1.

2.6. SQUID magnetometry

DC magnetization, M, was measured as a function of the applied magnetic field strength, H_a, and temperature, T, using a Superconducting Quantum Interference Device (SQUID) magnetometer (MPMS-5T from Quantum Design, San Diego, CA, USA), with the Reciprocating Sample Option (RSO). The experimental data were corrected by subtracting the paramagnetic signal of the sample holder (methacrylate bar with a notch for the sample) recorded at 10 K, above the superconducting critical temperature of Nb. The complex AC susceptibility, $\chi_{ac}(T)$, with in-phase χ' and out-of-phase χ'' components, was measured at zero DC magnetic field and AC drive magnetic field (sine wave of amplitude $\mu_0 h_0 = 10\,\mu T$ and frequency $f = 10$ Hz) in the same system, in order to determine the superconducting critical temperature (T_c), using the onset of diamagnetism criterion (full curves contained in the supplementary material section).

All magnetic measurements were performed on samples with size 3×3 mm^2 cut from the original films with the magnetic field parallel to the surface normal. In all cases the sample was cooled at zero magnetic field and, for each measurement, a reset of the superconducting magnet was performed previous to sample cool down in order to minimize the magnet's remnant field. Clone samples for the given laser treatment were fabricated and submitted to MOI and SQUID measurements respectively.

3. Results

3.1. Laser patterning

Guided by previous experience with Nb bulk and thin ribbon samples [19,20], our plan of action was devised as the two-step process described below. To start with, based on double-pulse irradiation we established the critical threshold parameters determining the onset of damage. With this boundary as a reference, we proceeded with the optimization of laser scanning parameters for treating the film's full surface and freezing the formation of LIPSS at a timely stage.

3.1.1. Definition of laser scanning parameters

Double pulse effects: determination of thresholds. In order to illustrate the application of the double-pulse method in our samples, Fig. 2 shows the micrographs of the upper film surface (100 nm film on Si substrate with Al caping layer) after irradiation with two different pulse energy values, E_p. The SEM images were taken by using the SE (Figs. 2a and b) and ESB detectors (Figs. 2c and d). It is worth mentioning that each laser pulse is well characterized by a gaussian energy distribution, with maximum value equal to $2E_p$ at $x = 0$, which explains the gradual increase of damage towards the center.

Corresponding to the zones labeled in the figure, the lower tables show the element analyses obtained by EDS, that clearly demonstrate the detrimental effect of increasing the radiation power above a certain limit. By increasing from $E_p = 4.6\,\mu J$ to $E_p = 6.4\,\mu J$, (corresponding pulse fluences $F_p = 0.27$ J/cm^2 and 0.38 J/cm^2, respectively) a dramatic effect is observed in the central part of the irradiated area, where a considerable amount of Nb is ablated. Thus, the atomic percentage of Nb decreases from 83% at the untreated surrounding area to 64% (left, pulse energy $4.6\,\mu J$) and to 36.4% (right, pulse energy $4.6\,\mu J$) at the center. The analysis of these micrographs also allows us to establish two relevant energy limits: (i) the minimum local energy able to affect the film surface, that is associated with the laser beam spot size; and (ii) the film damage threshold, which onsets the appearance of holes in the Nb layer (dark zones in the central area of Figs. 2c and d).

In these particular double-pulse conditions, it can be established that the local energy thresholds for surface modifications and for film damage are about $2.7\,\mu J$ and $8.3\,\mu J$, respectively, as marked by horizontal lines in the Gaussian profiles (Figs. 2e and f). Undoubtedly, these values may depend on the overlapping conditions and time delay between consecutive pulses, but they provide a very useful guide to find an optimal set of conditions for laser scanning processing, as discussed in the next section.

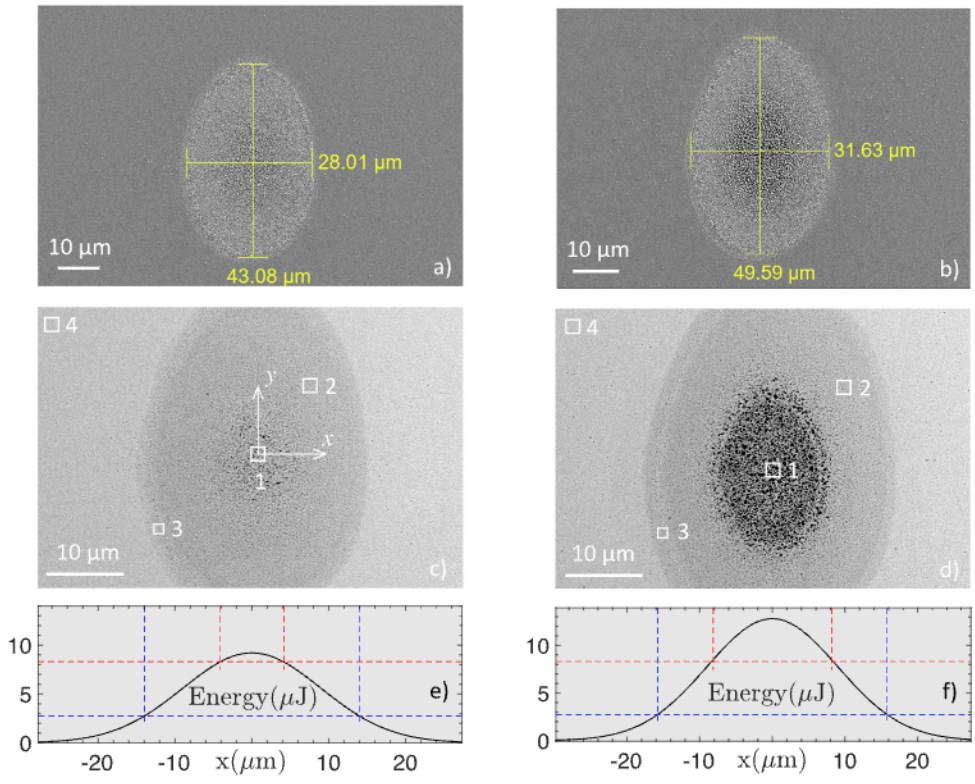

$E_p = 4.6\mu J$	O	Al	Si	Nb
1	5.5	0.8	28.8	64.8
2	7.1	*	10.4	82.5
3	8.7	4.2	3.8	83.4
4	4.6	8.6	3.4	83.3

$E_p = 6.4\mu J$	O	Al	Si	Nb
1	4.3	*	59.6	36.1
2	6.2	*	11.7	82.1
3	10.3	2.0	4.5	83.2
4	5.1	8.5	3.4	83.0

Fig. 2. SEM micrographs of the 100 nm Nb film irradiated with double pulses: left panels (a,c,e) E_p = 4.6 μJ (fluency F_p = 0.27 J/cm^2), right panels (b,d,f) E_p = 6.4 μJ (fluency F_p = 0.38 J/cm^2). Images correspond to SE (a,b) and ESB (c,d) detectors. (e) and (f) show the corresponding Gaussian profiles along the horizontal central axis (x), marking the threshold energy local values as explained in the text. The Labels 1, 2, 3, 4 in the intermediate panels (c,d) indicate specific areas (of size shown by the squares) where microanalysis was performed. Results (in atomic %) are shown in the accompanying tables. (*) means below detection level.

Laser scanning protocol optimization. We devised a protocol for covering the full surface of the samples, based on a meandering trajectory for the laser beam and appropriate overlapping between successive scans, schematically shown in Fig. 3. As it will be shown below, defining the overlapping conditions obeys a twofold purpose: (i) increasing uniformity at the intermediate scale (~100 μm), and (ii) achieving the formation of tailored LIPSS.

Following the analysis performed in Ref. [25], the optimum scan velocity v_L, as well as the hatching distance between consecutive lines δ_{lines}, were sought in agreement with the displacement between successive pulses $\delta_{pulses} = v_L/f_{rep}$, with f_{rep} the pulse repetition frequency, so as to obtain a homogeneous 2D accumulated fluence. In parallel, the effect of small variations of the individual pulse energy (below the previously established damage threshold) were investigated. Specifically, we studied combinations of v_L, δ_{lines}, E_p within the ranges 125 mm/s < v_L < 190 mm/s, 10 μm < δ_{lines} < 25 μm and 1.1 μJ < E_p < 4.4 μJ. As an example of the intermediate results in the optimization process, the reader may examine Fig. S1 (supplementary material). For the 100 nm sample, as shown in Fig. 3, the optimum conditions for the formation of LIPSS were identified to be: v_L = 125 mm/s, δ_{lines} = 10 μm, E_p = 2.6 μJ (F_p = 0.15 μJ/cm^2).

We call the readers' attention to the fact that, under the above conditions, one obtains a spatial overlap that is very similar for both directions, i.e.: $\delta_{pulses}/a \approx \delta_{lines}/b \approx 0.34$. In other words, the horizontal and vertical separation between laser spots is practically coincident in units relative to the semi-axes of the elliptical beam section. Nonetheless, one must bear in mind that the time scales are very different in both cases. The time elapsed between consecutive pulses within a line (50 μs) is three orders of magnitude shorter than between pulses in consecutive lines (≈24 ms, for lines scanning along the distance of 3 mm in our case). However, according to recent literature, the unexpected equivalence between the vertical and horizontal shifts finds an explanation in the fact that, ultimately, both time scales are much above the relaxation times related to the electron and lattice temperatures in the material [26,27], which can thus be considered as instantaneous processes.

The surface micrographs corresponding to the selected parameter values are shown in Fig. 3a and b. The nanopatterning characteristics are clearly visible. In particular, it is worth mentioning that the orientation of the LIPSS is perpendicular to the laser polarization, which, as shown, has a small deviation with respect to the horizontal axis. We recall that perpendicularity is characteristic of the so-called Low Spatial Frequency LIPSS, LSFL-I [13]. In agreement with the qualitative visual information, the 2D Fast Fourier Transform (FFT) analysis indicates an average period of the ripples $\Lambda \approx 250 \pm 5$ nm, and principal axes slightly deviated from the horizontal and vertical directions (by ≈9°).

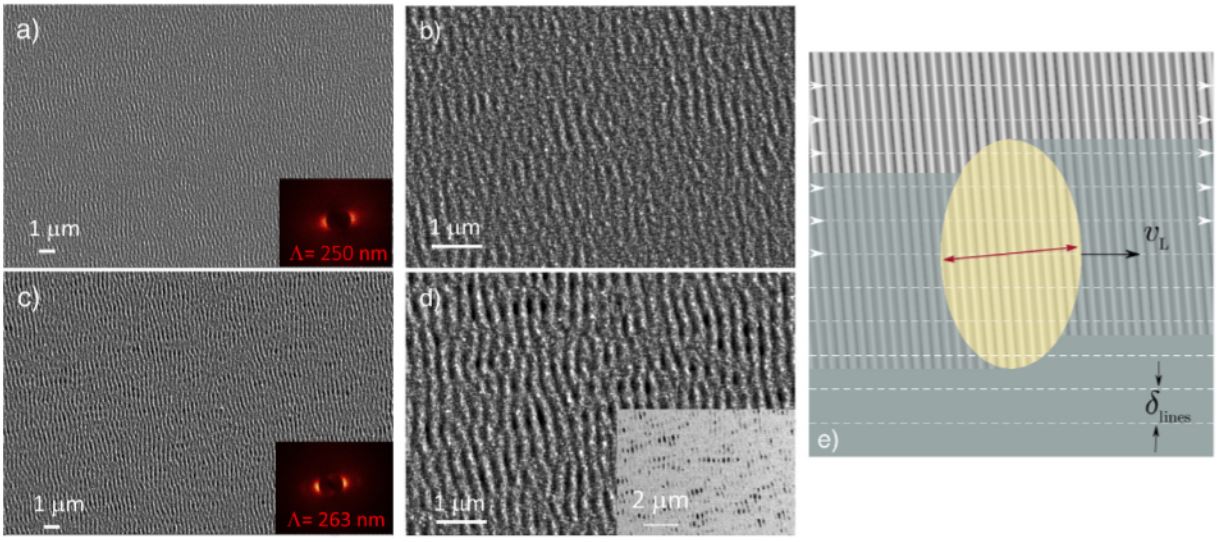

Fig. 3. SEM micrographs of the 100 nm sample after laser patterning by line scanning as indicated by the sketch to the right. (a) and (b) correspond to $E_p = 2.6\,\mu J$, while (c) and (d) are for $E_p = 3.4\,\mu J$. The left insets show the Fast Fourier Transform of the selected area. The inset in panel (d) corresponds to the ESB signal of the same area. As sketched in panel (e), for obtaining these structures, the laser spot scans the surface at a speed $v_L = 125$ mm/s, always rightwards and shifted by a distance $\delta_{lines} = 10\,\mu m$ in every step. The double arrow indicates the light polarization axis.

Table 1
Definition and basic properties of pristine and laser irradiated films using optimized parameters as explained in the text.

Sample	Thickness	T_c (K)	Sample	Thickness	T_c (K)
Nb1: pristine	100 nm	8.7	Nb2: pristine	200 nm	8.9
Nb1L: irradiated	100 nm	8.3	Nb2L: irradiated	200 nm	8.5

The determination of T_c is described in the following section.

This deviation is a constant for all the treatments, and is given by the misalignment between the polarization of the laser beam and the reference of the galvanometric optical system that shifts the beam. On the other hand, as an example of overtreatment features in the 100 nm-film can also be seen in Fig. 3c and d, corresponding to $E_p = 3.4\,\mu J$ and $F_p = 0.20$ J/cm^2. In this case, ripples were also formed with a similar spatial period ($\Lambda \approx 263 \pm 5$), but the presence of holes in the Nb layer is notorious, especially in the image taken with an ESB detector (inset), as it enhances the contrast between Nb (light gray) and Si (dark gray). As it was quantified by EDS on areas of $\approx 40 \times 55\ \mu m^2$, the atomic percentage of Nb for the optimum condition was determined as 78.5%, closely below the measured value of the untreated areas, whereas for the shown overtreated surface this value reduced significantly down to 59.2%. On the other hand, the atomic percentage of O increases from the pristine 4.0% to the 13.1% in the laser treated samples.

As shown in the supporting information (Fig.S2), for the same laser scanning conditions, SEM micrographs reveal very similar structures for the 200 nm sample, but for pulse energies slightly higher. Thus, the optimum pulse energy for the formation of LIPSS is $E_p = 3.0\,\mu J$.

Henceforth, the laser treated films using the above optimized parameters will be named as Nb1L and Nb2L, by comparison to pristine films (Nb1 and Nb2) as detailed in Table 1. This table also includes the values of the superconducting critical temperatures of the pristine and optimally irradiated films.

3.1.2. Topography of the surface

In order to determine the actual transverse profile of the periodic surface structures disclosed by SEM observations, TEM on lamellae extracted from the optimized laser patterned samples and AFM experiments for the characterization of larger areas were conducted (Fig. 4).

The lateral periodicity of the structures, and also the depth of the profiles can be clearly seen in TEM images (Fig. 4a,c). For further illustration, in the supplementary material section, we include images (Fig.S2) that show spots where the film was perforated due to overrated laser power.

AFM reveals undulations with lateral periodicities estimated at 260± 30 nm based on the spectral densities obtained through 2D FFT analysis of a $30 \times 30\,\mu m^2$ scanned area (depicted as top left insets in Fig. 4b,d). Topography profiles are also displayed, each spanning a length of 3 μm, averaged across 50 parallel lines within the region highlighted in the main panels. These profiles exhibit well-defined oscillations. The depth from crest to trough fluctuates around an average value of 20 nm, while the root mean square (RMS) roughness, calculated from $30 \times 30\,\mu m^2$ scanned areas, is approximately 16.5 nm for the 100-nm-thick sample and 18.5 nm for the laser treated 200-nm-thick sample, respectively. In order to highlight the laser patterning effect on the Nb films (already dressed with certain original topography), we include Fig.S3 in the supplementary material section, which shows that laser structuring is much above the pristine material roughness ($\lesssim$2 nm).

3.2. Magnetic properties

3.2.1. Magneto-optical Imaging

Fig. 5 shows the MOI signals corresponding to the penetration/exit of magnetic flux for the untreated/laser patterned samples. As further explained in the supplementary material section, (Fig.S4) these images indicate that superconducting currents flow isotropically for the original film and anisotropically in the laser treated samples. In fact, based on the critical state model (CSM) for flux penetration in superconductors [28,29], it is easy to show that the ratio of the critical current densities flowing in the platelet either perpendicular ($J_{c_\perp}$) or parallel ($J_{c_\parallel}$) to the LIPSS may be essentially found in terms of the angles defined by the clearly visible diagonals (so-called *d-lines*). In our case, for the laser treated samples, this gives

$$\frac{J_{c_\perp}}{J_{c_\parallel}} = \tan\vartheta \approx 0.32 \quad \text{for Nb1L (100 nm)}$$
$$\frac{J_{c_\perp}}{J_{c_\parallel}} = \tan\vartheta \approx 0.54 \quad \text{for Nb2L (200 nm)}. \qquad (1)$$

Thus, while the original films show isotropic magnetic flux penetration ($\tan(45°) = 1$), the laser treated samples with surface LIPSS display

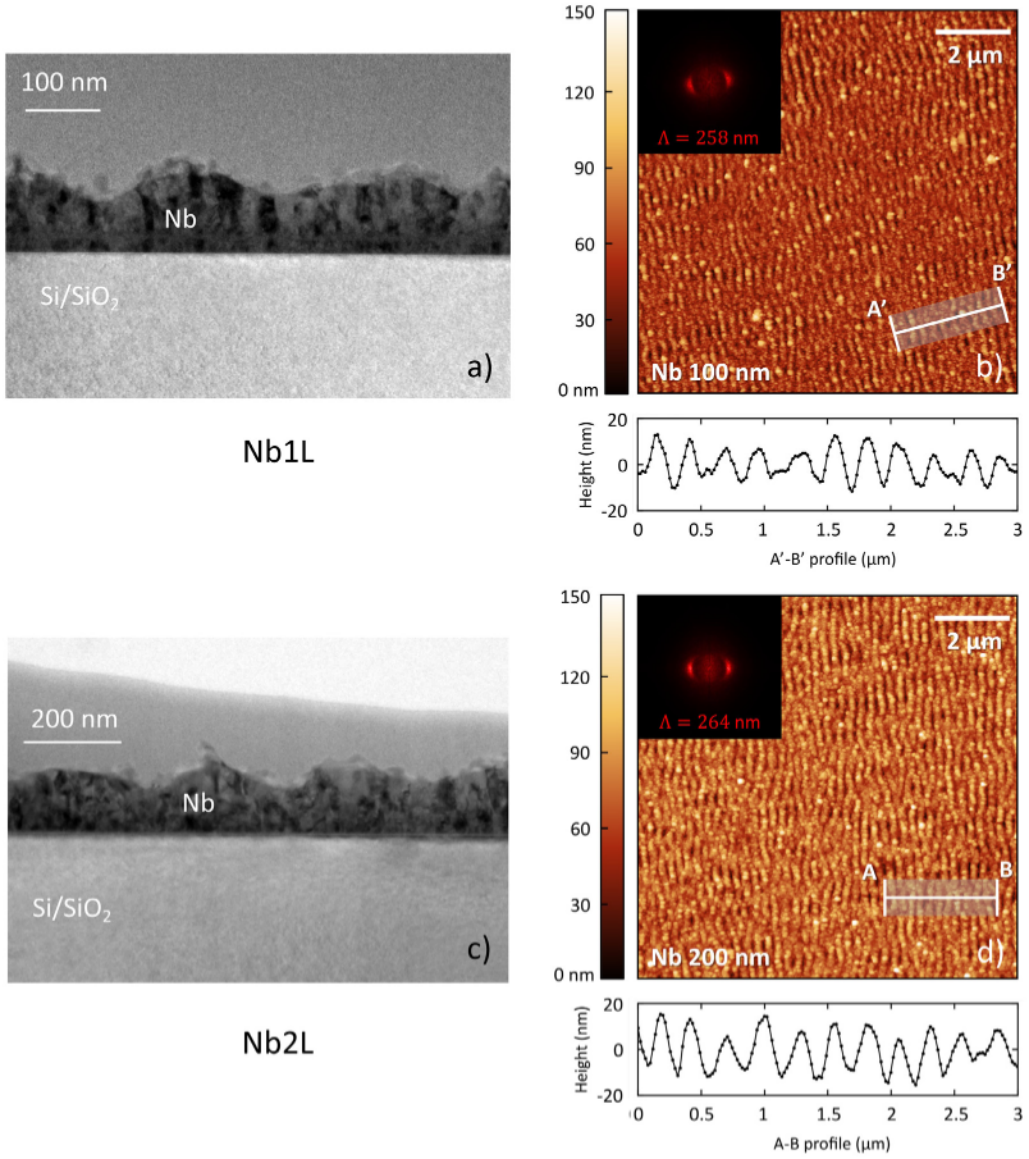

Fig. 4. Left: TEM images of the laser treated films. The substrate and the Nb layer are identified. Right: AFM topography color maps of the same samples in each row, both with a scan size of $10 \times 10\,\mu m^2$. Insets in the top left corner of each panel depict the spectral densities of the scanned surfaces. The bottom plots present the averaged surface profile along the highlighted segments indicated in the main panels. Panels (a) and (b) correspond to the laser treated 100 nm film (Nb1L) with the optimized pulse energy $E_p = 2.6\,\mu J$. Panels (c) and (d) are for the laser treated 200 nm film (Nb2L) with the optimized pulse energy $E_p = 3.0\,\mu J$.

a preferential penetration along the channels (and increased current density along them inasmuch as one has $\mu_0 \mathbf{J} = \mathbf{curl}\,\mathbf{B}$).

Hereafter, we will use the definition of the anisotropy coefficient $\gamma \equiv J_{c\parallel}/J_{c\perp}$, that represents the magnification factor in the critical current density. Strictly speaking, being related to the activation of vortex dynamics, this coefficient can depend on field and temperature. Here it will be taken as a roughly constant value for a given sample.

Further physical information of utter importance concerning the application of the thin films is contained in Fig. 5, panels (c),(f). As indicated by the selected images, the temperature dependence of the MOI response reveals a qualitatively different behavior for different temperature regimes. Note that, while flux penetration takes place rather smoothly and according to the isotropic/anisotropic current flow at the higher temperatures, the images at low temperatures show flux penetration in the form of dendritic avalanches. Notice that avalanches propagate preferentially along the direction transverse to the grooves (horizontal direction in the images) and eventually branch towards the vertical. It must be mentioned that flux avalanching behavior in superconductors has been extensively reported in the literature [30], and satisfactorily understood for thin films on the basis of thermomagnetic instability phenomena [31,32]. In brief, the essence of the phenomenon is explained through the higher level of electric power density in the region with higher current densities that triggers instabilities and initiates abrupt flux penetration [33]. In our case, the eventual systematic branching of the flux penetration paths towards the vertical direction adds a special feature, which is related to the surface patterning. A somewhat similar effect has been previously observed in superconducting films with artificial periodic pinning [34–37]. In short, the topography of the samples promotes the eventual flux channeling (in our case, along the orientation of the ripples).

The temperature dependence of the MOI intensity, shown in Fig. 5 benefits from the local resolution of the technique. Thus, by analyzing the intensity of the signal in a given region (for instance, along the heating process) one records the transition from the superconducting to the normal state and, in particular, obtains a local value for T_c (in fact, an average over the selected region). Technically, as the intensity of the signal is proportional to the magnetic flux density just over the sample B_z, and recalling that the magnetic moment of the superconductor

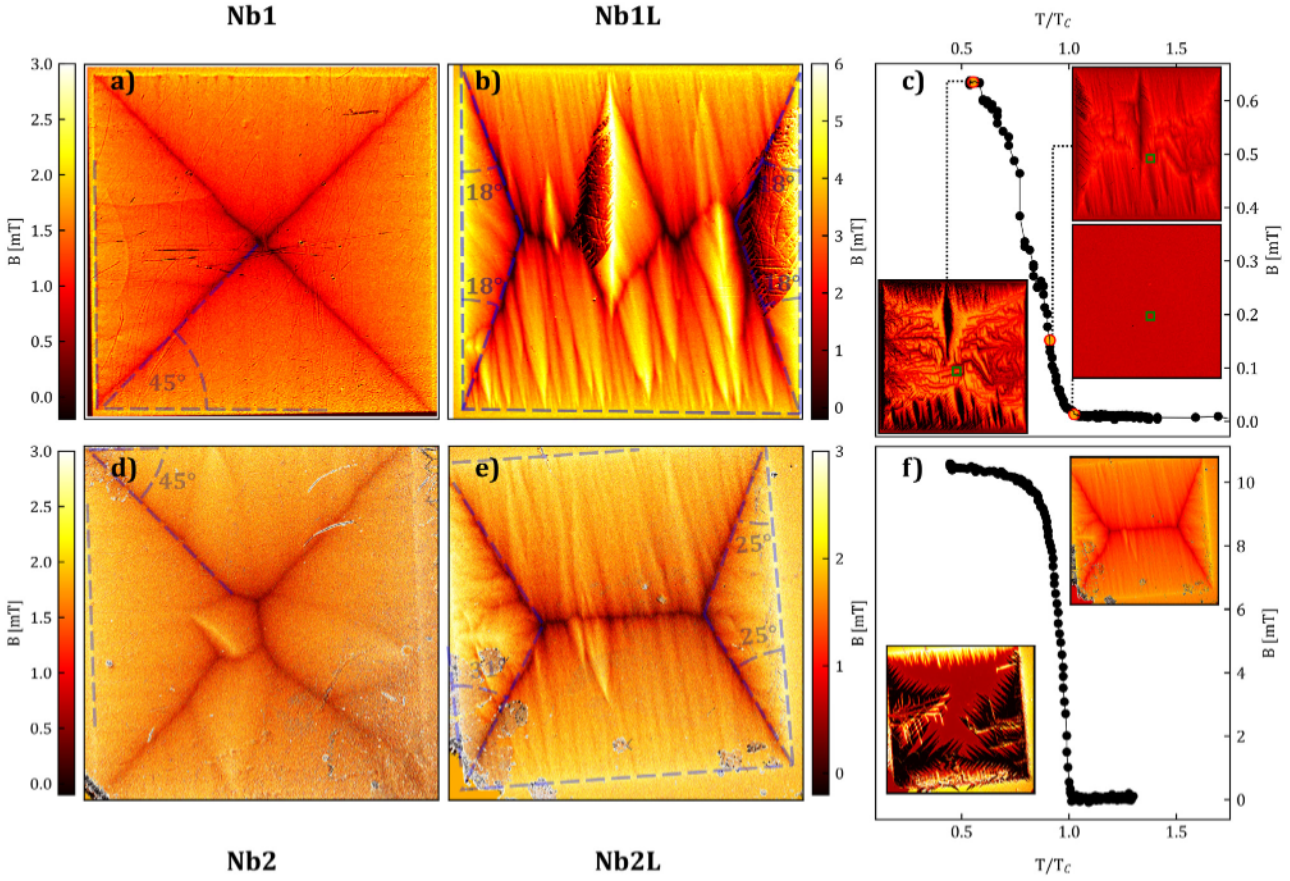

Fig. 5. Magneto-optical images of the pristine (Nb#) and laser-treated samples (Nb#L). Panels (a)–(c) correspond to the 100 nm film, and (d)–(f) are for the 200 nm film. (a) and (d) show the profiles for the pristine samples, while (b) and (e) are for the laser treated ones. Panels (a) and (b) show MOI images of the flux penetrated films after zero-field-cooling and subsequently applying a perpendicular magnetic field [(a) 3.8 K, 1.5 mT and (b) 6 K, 3.5 mT]. In Panel (c) the local magnetic field at the green box indicated in the insets, is monitored as a function of temperature. The initial state (lower left inset) corresponds to the remnant state after field-cooling with 4 mT down to the base temperature. MOI images for three selected temperatures are shown in the insets. The prominent vertical line in the MOI images for the laser treated sample was identified as a scratch on its surface. Panels (d) and (e) show MOI images of the flux penetrated films after zero-field-cooling and subsequently applying a perpendicular magnetic field of 2.1 mT. The temperature is 4 K for (d) and 7 K for (e). Panel (f) displays the evolution of the flux penetration patterns with temperature (see text). The lower inset shows an MOI image at base temperature for the Nb2L sample displaying avalanches whereas the upper inset shows that the avalanches are no longer present at high temperatures. In all cases, the orientation of the LIPSS coincides with the vertical direction.

relates to this value through the relation $\mu_0 M_z = \langle B_z \rangle - \mu_0 H_a$, the curves in Fig. 5 may be used to evaluate the out-of-plane component of the magnetic moment in the region of interest. Thus, by substracting the normal state reference (magnetic flux equals $\mu_0 H_a$) one roughly obtains the magnetization as a function of temperature $M(T)$. In our case, the plot corresponds to the remnant magnetic moment after field cooling and subsequently sweeping temperature up. Recall that, the larger the region analyzed, the closer the behavior to the macroscopic $M(T)$ dependence recorded in "conventional" volume magnetization measurements. In the following section, we present the behavior of the full samples' magnetic moment as obtained from SQUID magnetometer measurements.

3.2.2. SQUID magnetometry

Based on AC susceptibility, $\chi_{ac}(T)$ at zero DC magnetic field, we determined the superconducting critical temperatures, T_c of the samples, that are collected in Table 1 for the pristine and laser treated samples (detailed curves in supplementary material, Fig.S5).

DC magnetization curves at different values of the applied magnetic field strength, H_a, were recorded after zero field cooling the sample down to 2 K. Some interesting features were detected, as shown in Fig. 6, panel (a), that compares the temperature dependent magnetic moment for the pristine and laser treated samples at an applied field of 1 mT. For both sample thicknesses, the laser treated samples feature a higher magnetic moment for the range of higher temperatures (≈ between $T = 6$ K and $T = T_c$), while a reduced signal appears at lower temperatures. As it will be further confirmed, this is already an indication of the effect of laser patterning on the flux pinning/depinning mechanisms. An additional evidence of the role of the LIPSS structure relates to the appearance of broad bumps in the $M(T)$ curves at low temperatures (indicated by the arrows in Fig. 6). According to Ref. [38] this can be ascribed to the appearance of flux avalanching processes as those revealed in Fig. 5. Thus, inspired by these observations new experiments were performed in order to unveil the underlying physical mechanisms. In particular, isothermal magnetic hysteresis cycles were recorded in the range of temperatures $3\,\mathrm{K} < T < 7\,\mathrm{K}$, paying special attention at differences in the behavior above and below the crossover temperatures observed in $M(T)$. According to panel (b) in Fig. 5, the magnetic moment reduction for the patterned samples at low temperatures occurs concurrently with the appearance of non-smooth hysteresis cycles, showing sudden depletion of the sample's magnetization. As emphasized in the previous section, magnetic flux avalanching is a prominent feature in superconducting thin films, with clear fingerprints in MOI and with concomitant reduction of the sample's magnetic moment. Finally, we notice that the pristine films display a more stable behavior, just with some indication of avalanching at the lowest temperature ($T = 3$ K).

As for the case of higher temperatures, the field dependence $M(H)$, becomes more and more stable both in pristine and laser treated samples. Interestingly, the behavior as a function of the applied field

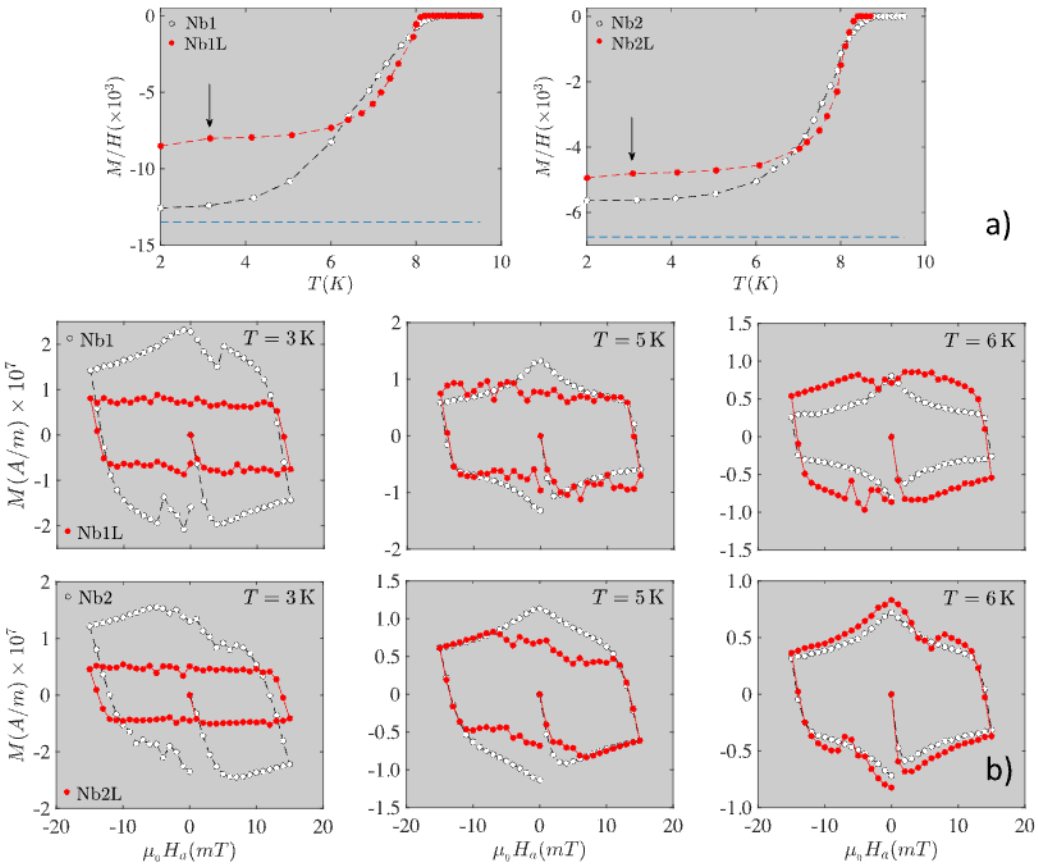

Fig. 6. Magnetization (ZFC conditions) of the pristine (white circles) and laser treated samples (colored circles). Panel (a): DC magnetic moment as a function of temperature for $\mu_0 H_a = 1$ mT. The horizontal lines indicate the ideal diamagnetic limit for the square film geometry. The vertical arrows point out the "bump" feature for the patterned samples (see text). Panel (b): isothermal $M(H)$ loops for the ZFC pristine and laser treated samples.

discloses a new feature, i.e.: the increased magnetic moment of the laser treated samples is not only bonded to the region of higher temperatures, but also limited by a maximum value of the magnetic field, above which pristine samples perform better. Thus, as marked in Fig. 7 a crossover between the higher performance of the pristine or laser treated samples is observed at fields $\mu_0 H^* \approx 60$ mT for the 100 nm sample and $\mu_0 H^* \approx 30$ mT for the 200 nm sample. We just recall that, according to Eq. (2) in the forthcoming section, in type-II superconductors, the critical current density is essentially given by the width of the hysteresis loop.

4. Discussion

In the previous sections, submicron LIPSS fabricated on Nb thin films have been demonstrated, with lateral periodicity around 250 nm and shallow enough to avoid perforation of the film (depth ≈ 20 nm). Concerning the superconducting properties of the laser treated samples, we first notice a faint reduction of the critical temperature ($\Delta T_c \approx 0.4$ K). This reduction appears together with an increase in the atomic percentage of oxygen in the irradiated samples, relative to the original composition (i.e.: to the native oxide layers). In fact, the reduction of T_c related to the presence of extra oxygen is well known for Nb [39,40], and in our case correlates to the laser irradiation process. Most significant is the observed topography induced anisotropy of the magnetic flux dynamics. In the smooth regime ($T \gtrsim 6K$), and according to Figs. 5 and 6, such a microstructure restrains the penetration of magnetic flux perpendicularly to the ripples, with concomitant modification of the electromagnetic response of the sample. This property has been quantified through MOI in terms of a well defined anisotropy of the critical current density for the laser treated samples, that also display an increased magnetic moment at higher temperatures. However, detrimental flux avalanching behavior at the lowest temperatures coexists with the enhanced performance closer to T_c. Below, we will put forward the interpretation of the experimental results presented above. Our discussion will rely on the so-called isothermal critical state model and the theory of magnetothermal instabilities in superconducting thin films.

Isothermal critical state model. The magnetic response of bulk superconductors to low frequency magnetic fields is customarily analyzed in terms of the so-called critical state model (CSM) [28,29]. In brief, the internal distribution of current and local magnetic field are obtained by solving the quasi-stationary Maxwell equations together with a material law $\mathbf{E}(\mathbf{J})$ for modeling losses when some threshold is exceeded. In the original Bean's model simplifying *ansatz*, the extreme relation $J = 0, \pm J_c$ is used, corresponding to the approximation of perfect conductivity for small currents ($E = 0$ for $J < J_c$), and arbitrarily high electric field for even the smallest excursion beyond the threshold J_c (critical current density of the material, a value that is instantly established for whatever a small electric field is induced). In a more general context, $\mathbf{E}(\mathbf{J}/J_c)$ has been modeled with different dependencies, with the so-called power-law model [41] ($E \propto J^n$) being one of the most celebrated. Different refinements of the well-established theory allow to incorporate the field-dependence of J_c [42,43] or anisotropy in specific forms. In any event, such models share the common feature that only electromagnetic quantities are involved. In other words, coupling to thermal modes does not enter the equations because heat evacuation to the bath is idealized, and one assumes a constant temperature (isothermal CSM). For our purposes, the CSM provides the framework that conceptualizes the experimental observations in the smooth regime. On the one hand, it provides a useful tool for analyzing MOI observations. In particular, it gives way to the analytical approximation leading to Eq. (1), that allows to obtain the anisotropy factor γ. On the other

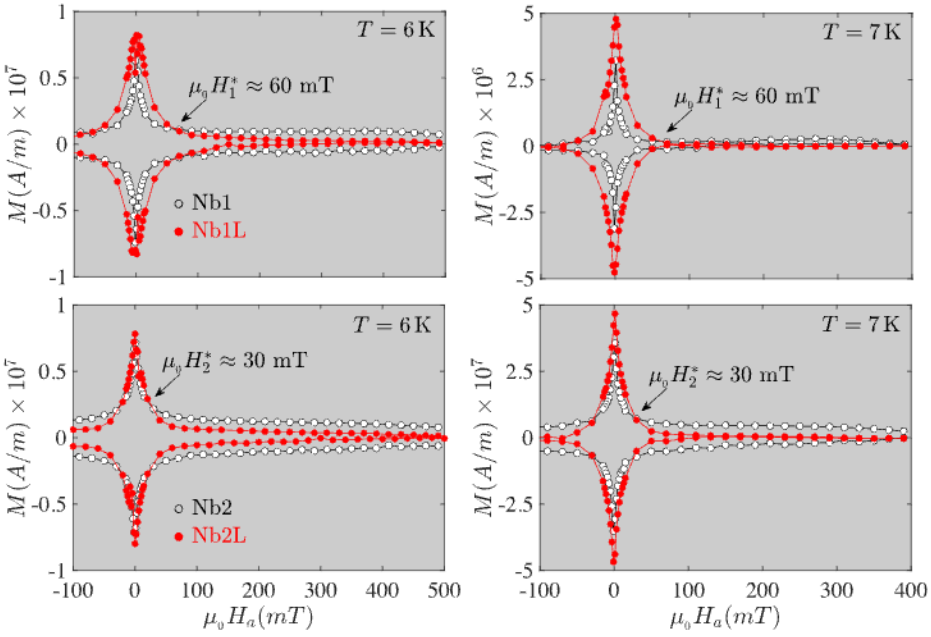

Fig. 7. Isothermal $M(H)$ loops for the ZFC pristine and laser treated samples at $T = 6$ K and $T = 7$ K. The arrows mark the experimentally observed crossover between the regimes of higher and lower critical current densities in the laser treated samples relative to the pristine ones. The experimental hysteresis loops have been trimmed in this plot in order to improve visualization. In fact, the unseen data may be guessed by symmetry.

hand, it establishes the link for the quantification of J_c from SQUID measurements. Thus, one may extract the critical current density from hysteresis loops in Fig. 6. We recall that one may use the celebrated approximation

$$J_c(B) \approx \frac{3}{2}\frac{\Delta M(\mu_0 H_a)}{a}, \tag{2}$$

in terms of the width of the magnetization loop $\Delta M \equiv M(H_a^{\mathrm{decr}}) - M(H_a^{\mathrm{incr}})$. This expression is an extrapolation from the theory for field-independent J_c valid for square platelets in a wide range of conditions. In our case (supplementary material, Fig.S6 and related discussion), this requires $H_a \gtrsim 1$ mT, and corresponds to the physical approximation $B \approx \mu_0 H_a$, i.e.: self-field effects may be neglected for the geometry under study. Note, for instance, that in view of Fig. 6, the application of this expression for the pristine 100 nm samples gives: $J_c(T = 5\,\mathrm{K}, \mu_0 H_a \lesssim 1\,\mathrm{mT}) \approx 2.5 \times 10^{10}\ \mathrm{A/m^2}$.

Concerning the influence of anisotropy in the overall magnetic response, we have derived the following expression

$$M_\gamma = M_{\mathrm{iso}}\frac{3 - 1/\gamma}{2} \tag{3}$$

that compares the saturation magnetic moment of the isotropic platelet (M_{iso}) and the anisotropic value in the case of field independent J_c. Note that this relation leads to $M_{\gamma=2}/M_{\mathrm{iso}} = 1.25$ and $M_{\gamma=3}/M_{\mathrm{iso}} = 1.33$. These values are compatible with the tendency observed in the measured magnetic moment per unit volume at the higher temperatures, as one can reckon in Figs. 6 and 7 together with the MOI experiments.

Magnetothermal instabilities. The observation of flux avalanching behavior both in MOI (Fig. 5) and SQUID measurements (Fig. 6) may be explained in the light of the so-called magnetothermal instability model, that has been used to produce Fig. 8, relying on actual typical values of the physical parameters for our Nb films. In brief, as it has been emphasized by many authors [31–33,36,37,44–46] and recently compiled in an extensive topical review [5], the smooth penetration in low-T_c superconducting thin films (Nb in particular) is intrinsically hampered by magnetothermal instabilities. Detrimental flux avalanches are promoted by the concurrence of low temperatures and high values of the critical current density, and may eventually end up with a very significant decay of the superconducting properties, as for instance the magnetic moment of the sample. A solid theoretical background for this phenomenon already exists, even enabling the description of the quantitative aspects [32]. Instabilities relate to the competition between two time scales, those controlling the magnetic flux diffusion (with accompanying heat generation) and the heat transfer (release) along the material and to the environment (in particular to the substrate). Thus, successful modeling of the flux dynamics has been reached by coupling the Maxwell equations, the superconducting material law, and the heat diffusion equation. Mostly significant is the fact that the main superconducting parameter is known to depend on field and temperature, i.e.: $J_c(\mathbf{B}, T)$. Then, the local current density may noticeably decrease if the combination of specific heat and thermal conductivities is such that local heat may not be timely released and temperature increases. Subsequently, the reduction of current density is accompanied by sudden flux penetration in those areas and a positive gain feedback loop begins. The probability of these processes increases at low temperatures and high values of the critical current density, because thermal conductivity diminishes with temperature and heat generation grows as $E \cdot J_c$.

In this work, the full description of flux avalanching (numerical in general, due to the intrinsic complexity) is not addressed. We restrict to the analytical evaluation of the expected conditions that initiate the avalanche process, more specifically, concerning the relevance of anisotropy in the critical current density for the observed instability. Following Refs. [31,32], the onset of the process may be established by a threshold value for the magnetic field penetration distance $\ell^*(T, P_{\mathrm{sc}})$, for a given temperature, and also related to a number of superconducting parameters P_{sc} including the thermal conductivity, heat transfer coefficient to the substrate and critical current density. Additionally, one may use the CSM model expression that connects the penetration distance and the applied magnetic field $\ell(H_a)$ for thin superconducting strips and invert it to reach an expression of a threshold magnetic field in terms of the material parameters. In particular, one may evaluate the J_c–dependence of the threshold field (displayed in Fig. 8) at which instabilities are presumed to appear for a given temperature. For the case of a thin superconducting strip (width $2w$, thickness d), one may define a threshold value for the magnetic flux penetration depth at which the sample becomes unstable and dendritic flux penetration

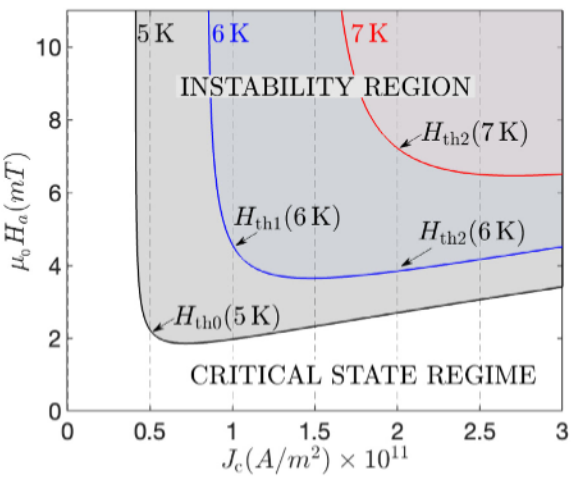

Fig. 8. Theoretical magnetothermal stability diagram, based on typical parameter values for our Nb films. Shown are the threshold lines for temperatures $T = 5, 6, 7$ K separating the stable CSM regime (below each line) and the upper region of instability. Several transition field values $\mu_0 H_{th}$ to the instability region are marked for $J_c = 0.5\times10^{11}$ A/m^2 (H_{th0}), $J_c = 10^{11}$ A/m^2 (H_{th1}), and for $J_c = 2\times10^{11}$ A/m^2 (H_{th2}).

begins. It is given by [32]

$$\ell^* = \frac{\pi}{2}\sqrt{\frac{kT^*}{J_c E}}\left(1-\sqrt{\frac{2hT^*}{ndJ_c E}}\right)^{-1}. \tag{4}$$

This expression includes the material parameters:

k : thermal conductivity of the superconductor (temperature dependent).

J_c : critical current density (temperature dependent).

$T^* \equiv -(\partial \ln J_c/\partial T)^{-1}$.

E : characteristic electric field value for the development of instability.

h : heat transfer coefficient to substrate (temperature dependent).

n : exponent in the E(J) power law ($E \propto J^n$) (temperature dependent).

d : thickness of the film.

In Eq. (4), the temperature dependencies are taken to be [32,46]

$$\begin{aligned} k(T) &= k_0(T/T_c)^3 \\ J_c(T) &= J_{c0}(1-T/T_c) \\ h(T) &= h_0(T/T_c)^3 \\ n(T) &= n_0(T/T_c). \end{aligned} \tag{5}$$

In order to generate a phase diagram representative for our Nb films, Fig. 8 has been obtained by using the following values (Refs.[32,46] and our measurements): $k_0 = 20$ W/K m, $J_{c0} \sim 10^{11}$ A/m^2, $h_0 = 1.0\times10^4$ W/K m^2, $n_0 = 30$, $d = 100$ nm, $E = 200$ mV/m, $T_c = 8.3$ K.

Eventually, the threshold that defines the transition between the stable/unstable regimes is evaluated by inserting Eq. (4) in the following expression, that relates the flux penetration depth ℓ with the applied magnetic field intensity $\mathbf{H}_a$ perpendicular to the surface of the strip [47]

$$H_a = \frac{J_c d}{\pi}\operatorname{arccosh}\left(\frac{W}{W-\ell}\right). \tag{6}$$

Interpretation of the magnetic behavior. According to Fig. 5, in the smooth critical state regime, patterned samples display anisotropic behavior quantified by the relation $J_{c_\parallel} \approx 3J_{c_\perp}$ for the case of the 100 nm sample and $J_{c_\parallel} \approx 2J_{c_\perp}$ for the case of the 200 nm sample. Then, considering for instance the former case, and by applying relations (2) and (3) to our experimental data, one gets $J_{c_\perp} \approx 0.25\times10^{11}$ A/m^2 and $J_{c_\parallel} \approx 0.75\times10^{11}$ A/m^2 at $T = 5$ K (and $\mu_0 H_a \lesssim 1$ mT). We note that, according to the discussion that follows Eq. (3), our experimental data (MOI together with SQUID measurements) support that $J_{c_\perp}$ basically equals the isotropic value ($J_{c,iso}$), while $J_{c_\parallel}$ is multiplied by the anisotropy factor γ. Physically, the effect of undulating the surface retards vortex depinning across the channels and does not essentially modify it along them.

In view of Fig. 6b, and taking the above values into account, one may explain that pristine samples are stable at 5 K and laser treated samples fall into the instability zone for $\mu_0 H_a$ in the range of a few mT at 5 K and 6 K, and instability begins in the form of dendrites in the lateral sides where current flows along the Y-axis (see Fig.S4 for a graphical representation). On the other hand, for $T > 6$ K both the pristine and patterned samples behave smoothly in the full range of applied fields as confirmed in $M(H)$ measurements. In view of this, together with the observation of the enhanced flux penetration along the ripples, there is room for devising flux channeling applications in the range of a few mT and temperatures $T \gtrsim 6$ K.

5. Concluding remarks

Laser irradiation with ultra-short pulses has been demonstrated to be an enabling technology for nanopatterning the surface of superconducting thin films. For this study, superconducting Nb thin films with thicknesses of 100 nm and 200 nm deposited on top of Si substrates were processed with a Yb:KGW laser of wavelength $\lambda = 343$ nm, and pulses of duration 238 fs. Surface structures with quasi-parallel ripples (so-called LIPSS) were obtained by optimizing the laser parameters. Our main focus was on the control of the LIPSS formation kinetics, so as to avoid perforation of the film, while still obtaining a well defined periodic surface structure capable of modulating the superconducting properties. The laser power, repetition frequency, scanning speed and overlap between successive lines play an essential role in the process. Relying on previous experience in bulk samples of different metals, we could find a combination of parameters that give way to surface nanopatterned films.

The topography of the surface, the depth of the undulations and the elemental composition were consistently established by SEM and TEM with elemental analysis, and AFM observations. Ripples of lateral separation ≈250 nm and average depth of ≈20 nm were achieved both in the patterned 100 nm and 200 nm films.

According to the magneto-optical studies and SQUID magnetometry performed on pristine and laser treated samples, the obtained undulations produce an anisotropic behavior. From MOI analysis, the critical current density along the surface channels basically duplicates/triplicates the value along the transverse direction for the 200 nm/100 nm sample. Correspondingly, the magnetic flux penetrates with more ease (duplicates/triplicates distance in a given step) along the channels. On the other hand, laser patterning improves the global magnetization of the films for the region of higher temperatures ($5\,K < T < T_c$) and moderate/low magnetic fields ($\mu_0 H_a \lesssim 0.1$ T), but worsens outside this range. The crossover between the regions of improved/depressed superconductivity by the laser treatment is herein explained in terms of the anisotropic current flow in combination with the thermal conduction properties of the film. In consonance with previous studies, an enhanced critical current density leads to more unstable behavior at low temperatures and high fields (as compared to pristine samples) because a positive feedback between heat generation and the impossibility to evacuate heat occurs and superconductivity is locally destroyed.

Finally, it is worth mentioning that the versatility of the laser processing technique paves the way to a rich scenario of pattern modeling on the surface of superconducting thin films. Essentially, having a spot of typical size $\lesssim$50 μm one can design a wealth of microscopic scale configurations over the film, with LIPSS oriented according to the polarization of the laser beam. This enables the possibility of creating circuits either for injecting or driving magnetic flux to specified points and may be a useful tool in fluxonic devices as well as relevant for post-processing superconducting radiofrequency resonators with tailored pinning landscapes.

CRediT authorship contribution statement

Antonio Badía-Majós: Conceptualization, Formal analysis, Investigation, Software, Visualization, Writing – original draft, Writing – review & editing. **Elena Martínez:** Conceptualization, Data curation, Formal analysis, Investigation, Writing – review & editing. **Luis A. Angurel:** Conceptualization, Funding acquisition, Investigation, Supervision, Writing – review & editing. **Germán F. de la Fuente:** Conceptualization, Formal analysis, Investigation, Writing – review & editing. **Emile Fourneau:** Conceptualization, Data curation, Investigation, Methodology, Visualization, Writing – review & editing. **Stefan Marinković:** Conceptualization, Data curation, Investigation, Visualization, Writing – review & editing. **Alejandro V. Silhanek:** Conceptualization, Formal analysis, Funding acquisition, Investigation, Methodology, Supervision, Writing – review & editing.

Declaration of competing interest

The authors declare that they have no known competing financial interests or personal relationships that could have appeared to influence the work reported in this paper.

Data availability

The experimental data that support the findings of this study are openly available in [ZENODO] at [https://doi.org/10.5281/zenodo.10245401]. Simulation software is available upon request to the authors.

Acknowledgments

The authors gratefully acknowledge the financial support from Spanish MCIN/AEI/10.13039/501100011033 (project PID2020-113034RB-I00), Gobierno de Aragón(research group T54_23R). The work of A.V. Silhanek and E. Fourneau has been financially supported by the Fonds de la Recherche Scientifique - FNRS under the grants Excellence of Science (EOS) project O.0028.22 and PDR T.0204.21. S. Marinković acknowledges support from FRS-FNRS (Research Fellowships ASP). A. Badía-Majós wants to acknowledge partial financial support from the European Union under Hi-Scale COST action (CA19108). The authors also would like to acknowledge the use of Servicio General de Apoyo a la Investigación-SAI and Laboratorio de Microscopías Avanzadas, Universidad de Zaragoza.

Appendix A. Supplementary data

Supplementary material related to this article can be found online at https://doi.org/10.1016/j.apsusc.2023.159164.

References

[1] J. Eisenstein, Superconducting elements, Rev. Modern Phys. 26 (1954) 277–291.
[2] D.K. Finnemore, T.F. Stromberg, C.A. Swenson, Superconducting properties of high-purity niobium, Phys. Rev. 149 (1966) 231–243.
[3] R. Prozorov, M. Zarea, J.A. Sauls, Niobium in the clean limit: An intrinsic type-I superconductor, Phys. Rev. B 106 (2022) L180505.
[4] S. Marinković, E.A. Abbey, D.A.D. Chaves, S. Collienne, E. Fourneau, L. Jiang, C. Xue, Y.H. Zhou, W.A. Ortiz, M. Motta, N.D. Nguyen, A. Volodin, J. Van de Vondel, A.V. Silhanek, Effect of moderate electropulsing on Nb multiterminal transport bridges, Phys. Rev. A 19 (2023) 054009.
[5] F. Colauto, M. Motta, W.A. Ortiz, Controlling magnetic flux penetration in low-Tc superconducting films and hybrids, Supercond. Sci. Technol. 34 (1) (2020) 013002.
[6] A.M. Kadin, Duality and fluxonics in superconducting devices, J. Appl. Phys. 68 (11) (1990) 5741–5749.
[7] J.E. Villegas, S. Savel'ev, F. Nori, E.M. González, J.V. Anguita, R. García, J.L. Vicent, A superconducting reversible rectifier that controls the motion of magnetic flux quanta, Science 302 (5648) (2003) 1188–1191.
[8] O.V. Dobrovolskiy, M. Huth, Dual cut-off direct current-tunable microwave low-pass filter on superconducting Nb microstrips with asymmetric nanogrooves, Appl. Phys. Lett. 106 (14) (2015) 142601.
[9] V.K. Vlasko-Vlasov, F. Colauto, T. Benseman, D. Rosenmann, W.K. Kwok, Triode for magnetic flux quanta, Sci. Rep. (1) (2016) 36847.
[10] M. Birnbaum, Semiconductor surface damage produced by ruby lasers, J. Appl. Phys. 36 (11) (1965) 3688–3689.
[11] H.M. van Driel, J.E. Sipe, J.F. Young, Laser-induced periodic surface structure on solids: A universal phenomenon, Phys. Rev. Lett. 49 (1982) 1955–1958.
[12] S. Höhm, A. Rosenfeld, J. Krüger, J. Bonse, Area dependence of femtosecond laser-induced periodic surface structures for varying band gap materials after double pulse excitation, Appl. Surf. Sci. 278 (2013) 7–12, Laser materials processing for micro and nano applications, E-MRS 2012 Symposium V.
[13] J. Bonse, S. Höhm, S.V. Kirner, A. Rosenfeld, J. Krüger, Laser-induced periodic surface structures— A scientific evergreen, IEEE J. Sel. Top. Quantum Electron. 23 (3) (2017).
[14] J. Bonse, Quo vadis LIPSS?—Recent and future trends on laser-induced periodic surface structures, Nanomaterials 10 (10) (2020).
[15] W. Karim, A. Petit, E. Millon, J. Vulliet, M. Tabbal, A.L. Thomann, N. Semmar, Nano-squares and regular LIPSS on YSZ coating by picosecond UV laser beam: Thin film mediated and direct texturing, Appl. Surf. Sci. 623 (2023) 157110.
[16] H. Raether, Surface Plasmons on Smooth and Rough Surfaces and on Gratings, Springer Tracts in Modern Physics, Vol. 111, Springer Berlin, Heidelberg, 1988.
[17] F. Fraggelakis, G.D. Tsibidis, E. Stratakis, Tailoring submicrometer periodic surface structures via ultrashort pulsed direct laser interference patterning, Phys. Rev. B 103 (2021) 054105.
[18] A. Pan, A. Dias, M. Gómez-Aranzadi, S.M. Olaizola, A. Rodríguez, Formation of laser-induced periodic surface structures on niobium by femtosecond laser irradiation, J. Appl. Phys. 115 (17) (2014) 173101.
[19] A. Cubero, E. Martínez, L.A. Angurel, G.F. de la Fuente, R. Navarro, H. Legall, J. Krüger, J. Bonse, Effects of laser-induced periodic surface structures on the superconducting properties of Niobium, Appl. Surf. Sci. 508 (2020) 145140.
[20] A. Cubero, E. Martínez, L.A. Angurel, G.F. de la Fuente, R. Navarro, H. Legall, J. Krüger, J. Bonse, Surface superconductivity changes of niobium sheets by femtosecond laser-induced periodic nanostructures, Nanomaterials 10 (12) (2020) 2525.
[21] A. Rodríguez, M.C. Morant-Miñana, A. Dias-Ponte, M. Martínez-Calderón, M. Gómez-Aranzadi, S.M. Olaizola, Femtosecond laser-induced periodic surface nanostructuring of sputtered platinum thin films, Appl. Surf. Sci. 351 (2015) 135–139.
[22] J. Evertsson, F. Bertram, F. Zhang, L. Rullik, L. Merte, M. Shipilin, M. Soldemo, S. Ahmadi, N. Vinogradov, F. Carlà, J. Weissenrieder, M. Göthelid, J. Pan, A. Mikkelsen, J.-O. Nilsson, E. Lundgren, The thickness of native oxides on aluminum alloys and single crystals, Appl. Surf. Sci. 349 (2015) 826–832.
[23] J.M. Liu, Simple technique for measurements of pulsed Gaussian-beam spot sizes, Opt. Lett. 7 (5) (1982) 196–198.
[24] G. Shaw, J. Brisbois, L.B.G.L. Pinheiro, J. Müller, S. Blanco Alvarez, T. Devillers, N.M. Dempsey, J.E. Scheerder, J. Van de Vondel, S. Melinte, P. Vanderbemden, M. Motta, W.A. Ortiz, K. Hasselbach, R.B.G. Kramer, A.V. Silhanek, Quantitative magneto-optical investigation of superconductor/ferromagnet hybrid structures, Rev. Sci. Instrum. 89 (2) (2018) 023705.
[25] L. Porta-Velilla, N. Turan, A. Cubero, W. Shao, H. Li, G.F. de la Fuente, E. Martínez, A. Larrea, M. Castro, H. Koralay, S. Cavdar, J. Bonse, L.A. Angurel, Highly regular hexagonally-arranged nanostructures on Ni-W alloy tapes upon irradiation with ultrashort UV laser pulses, Nanomaterials 12 (14) (2022) 2380.
[26] G. Tsibidis, D. Mansour, E. Stratakis, Damage threshold evaluation of thin metallic films exposed to femtosecond laser pulses: The role of material thickness, Opt. Laser Technol. 156 (2022) 108484.
[27] F. Fraggelakis, P. Lingos, E. Cusworth, V.G. Kravets, A.N. Grigorenko, A.V. Kabashin, E. Stratakis, Highly ordered LIPSS on Au thin film for plasmonic sensing fabricated by double femtosecond pulses, 2023, Preprint. arXiv:2303.03180.
[28] C.P. Bean, Magnetization of hard superconductors, Phys. Rev. Lett. 8 (6) (1962) 250–253.
[29] C.P. Bean, Magnetization of high-field superconductors, Rev. Modern Phys. 36 (1) (1964) 31–39.
[30] P.S. Swartz, C.P. Bean, A model for magnetic instabilities in hard superconductors: The adiabatic critical state, J. Appl. Phys. 39 (11) (1968) 4991–4998.
[31] D.V. Denisov, A.L. Rakhmanov, D.V. Shantsev, Y.M. Galperin, T.H. Johansen, Dendritic and uniform flux jumps in superconducting films, Phys. Rev. B 73 (2006) 014512.
[32] D.V. Denisov, D.V. Shantsev, Y.M. Galperin, E.-M. Choi, H.-S. Lee, S.-I. Lee, A.V. Bobyl, P.E. Goa, A.A.F. Olsen, T.H. Johansen, Onset of dendritic flux avalanches in superconducting films, Phys. Rev. Lett. 97 (2006) 077002.
[33] J. Albrecht, A.T. Matveev, J. Strempfer, H.-U. Habermeier, D.V. Shantsev, Y.M. Galperin, T.H. Johansen, Dramatic role of critical current anisotropy on flux avalanches in MgB_2 films, Phys. Rev. Lett. 98 (2007) 117001.
[34] M. Menghini, R.J. Wijngaarden, A.V. Silhanek, S. Raedts, V.V. Moshchalkov, Dendritic flux penetration in Pb films with a periodic array of antidots, Phys. Rev. B 71 (2005) 104506.

[35] M. Motta, F. Colauto, J.I. Vestgården, J. Fritzsche, M. Timmermans, J. Cuppens, C. Attanasio, C. Cirillo, V.V. Moshchalkov, J. Van de Vondel, T.H. Johansen, W.A. Ortiz, A.V. Silhanek, Controllable morphology of flux avalanches in microstructured superconductors, Phys. Rev. B 89 (2014) 134508.

[36] M. Motta, L. Burger, L. Jiang, J.D. González Acosta, Z.L. Jelić, F. Colauto, W.A. Ortiz, T.H. Johansen, M.V. Milosević, C. Cirillo, C. Attanasio, C. Xue, A.V. Silhanek, B. Vanderheyden, Metamorphosis of discontinuity lines and rectification of magnetic flux avalanches in the presence of noncentrosymmetric pinning forces, Phys. Rev. B 103 (2021) 224514.

[37] P. Mikheenko, M. Jacquemin, M. Mojarrad, F. Mercier, Controlling dendritic flux avalanches by nanostructure of superconducting films, in: 2022 IEEE 12th International Conference Nanomaterials: Applications & Properties (NAP), 2022, pp. SNMS01–1–SNMS01–5.

[38] A.V. Silhanek, S. Raedts, V.V. Moshchalkov, Paramagnetic reentrance of ac screening: Evidence of vortex avalanches in Pb thin films, Phys. Rev. B 70 (2004) 144504.

[39] J. Halbritter, On the oxidation and on the superconductivity of niobium, Appl. Phys. A 43 (1) (1987) 1–28.

[40] M. Grundner, J. Halbritter, XPS and AES studies on oxide growth and oxide coatings on niobium, J. Appl. Phys. 51 (1) (2008) 397–405.

[41] J. Rhyner, Magnetic properties and AC-losses of superconductors with power law current—voltage characteristics, Phys. C: Supercond. 212 (3) (1993) 292–300.

[42] Y.B. Kim, C.F. Hempstead, A.R. Strnad, Magnetization and critical supercurrents, Phys. Rev. 129 (2) (1963) 528–535.

[43] D.X. Chen, R.B. Goldfarb, Kim model for magnetization of type-II superconductors, J. Appl. Phys. 66 (6) (1989) 2489–2500.

[44] J.I. Vestgården, P. Mikheenko, Y.M. Galperin, T.H. Johansen, Nonlocal electrodynamics of normal and superconducting films, New J. Phys. 15 (9) (2013) 093001.

[45] F. Colauto, D. Carmo, A.M.H. de Andrade, A.A.M. Oliveira, W.A. Ortiz, T.H. Johansen, Anisotropic thermomagnetic avalanche activity in field-cooled superconducting films, Phys. Rev. B 96 (2017) 060506.

[46] L. Jiang, C. Xue, L. Burger, B. Vanderheyden, A.V. Silhanek, Y. Zhou, Selective triggering of magnetic flux avalanches by an edge indentation, Phys. Rev. B 101 (2020) 224505.

[47] E.H. Brandt, M. Indenbom, Type-II-superconductor strip with current in a perpendicular magnetic field, Phys. Rev. B 48 (17) (1993) 12893–12906.